A Study of Cr_3C_2-Based HVOF and HVAF Sprayed Coatings: Microstructure and Carbide Retention

V. Matikainen[1]*, G. Bolelli[2], H. Koivuluoto[1], M. Honkanen[1], M. Vippola[1], L. Lusvarghi[2] and P. Vuoristo[1]

[1] Tampere University of Technology, Laboratory of Materials Science, Tampere, Finland.

[2] University of Modena and Reggio Emilia, Modena, Italy.

**E-mail: ville.matikainen@tut.fi*

1. ABSTRACT

The research on high velocity air-fuel (HVAF) sprayed Cr_3C_2-based materials has mostly focused on conventional Cr_3C_2-25NiCr composition. In this paper, two alternative compositions (Cr_3C_2-50NiCrMoNb and Cr_3C_2-37WC-18NiCoCrFe) were sprayed with high velocity oxy-fuel (HVOF) and HVAF spray processes to evaluate the material behaviour during spraying and to provide characterisation of the microstructures and mechanical properties of the coatings. For comparison, coatings from the Cr_3C_2-25NiCr composition were sprayed with both processes. Spray diagnostics were carried out to obtain average particle velocity and temperature for each material and process combinations. The measured average in-flight particle data was 1800 °C and 700 m/s for HVOF process, and 1450 °C and 900 m/s for HVAF process.

Characterisation of the coating microstructures was carried out by scanning electron microscopy and X-ray diffraction. In addition, the carbon content of the feedstock powders and sprayed coatings was measured with carbon analyser. The results show that carbide rebounding or selective deposition of particles with higher metal matrix content is the dominating reason for carbide loss during HVAF spraying, while carbide dissolution is an additional source for the HVOF spraying. Higher particle velocities and controlled temperature measured for the HVAF process produced dense coatings with improved toughness and more homogenous coating structure.

2. INTRODUCTION

Chromium carbide (Cr_3C_2)-based materials are used as wear resistant coatings (Ref 1–3) in numerous industrial applications due to their good oxidation resistance (Ref 4), corrosion resistance (Ref 5) and low coefficient of friction at high temperatures (Ref 6,7). One of the most common compositions is the Cr_3C_2-25NiCr in which the hard Cr_3C_2 particles are embedded in a ductile Ni20Cr metal matrix. The material is used as thermally sprayed coating especially at elevated temperatures, e.g. in power generation (Ref 8), where the harsh operation environment can involve a combination of elevated temperature, corrosion and wear (Ref 9). At lower temperatures, on the other hand, harder tungsten carbide (WC)-based coatings have better wear resistance (Ref 1,10,11).

Several commercial Cr_3C_2-based materials have been designed to provide improved corrosion or wear resistance compared to the standard Cr_3C_2-25NiCr composition. The corrosion resistance and ductility of the Cr_3C_2-based coatings can potentially be improved by increasing the metallic matrix content. One of such commercial materials is Cr_3C_2-50NiCrMoNb (Ref 12). On the other hand, the wear resistance of the typical Cr_3C_2-25NiCr coatings can be improved by replacing some of the Cr_3C_2 particles with harder WC particles, e.g. Cr_3C_2-37WC-18NiCoCrFe (Ref 13). Evenly distributed fine WC particles strengthen the coating and provide increased hardness, while the higher density of the material can potentially increase the kinetic energy of the particles and improve coating compaction. However, the microstructure of the hardmetal coating and the degree of decarburization are affected by the spray process and the feedstock type (Ref 14–16). Currently, HVOF is the most commonly used process for spraying hardmetals.

After the breakthrough of the HVOF spray process in the early 90s, the development has focused on modifications of these systems (Ref 17–19) and on the development of high velocity air-fuel (HVAF) spray process. Especially the modern gaseous fuel HVAF spraying has attracted growing interest during the last decade by providing a lower temperature spray process (Ref 20) capable of reaching high powder feed rates (Ref 21,22). A fraction of the particles is typically overheated during HVOF spraying by the high temperature combustion, which leads to carbide dissolution (Ref 14). This effect can be significantly

reduced with the HVAF spray process (Ref 23,24). Therefore, it is of high interest to study the behaviour of Cr_3C_2-based materials sprayed with both HVOF and HVAF spray processes.

While there are several studies carried out with the early models of the gaseous fuel HVAF spray processes (Ref 21,22,25), the particle velocities with such equipment have been reported to reach 700-800 m/s for WC-CoCr powder (Ref 21,25). It has already been reported that by using convergent-divergent nozzle designs, particle velocities of over 900 m/s can be achieved with the modern HVAF spray process (Ref 20). Comparative studies between the HVOF and HVAF spray processes have already been done, but they have mostly focused on WC-based materials and lack the particle in-flight data (particle velocity and temperature) (Ref 23,24). Recently a study focusing on sliding wear behaviour of HVOF and HVAF sprayed Cr_3C_2-25NiCr coatings was published (Ref 11) and another one included also WC alloyed alternative coatings such as Cr_3C_2-10WC-10Ni and Cr_3C_2-37WC-18NiCoCrFe (Ref 26). However, there is a need to incorporate spray diagnostics and further characterization of the alternative Cr_3C_2-based materials. Findings on the HVAF sprayed coatings of such materials were reported in our previous work (Ref 27). In the current study, different Cr_3C_2-based materials were sprayed with HVOF and HVAF spray processes in order to compare the material behaviour during deposition. In addition, average particle velocities and temperatures were measured in order to provide valuable data for the comparison of the two spray processes. Coatings were analysed to study the process effect on the structures of different Cr_3C_2-based coating materials.

3. EXPERIMENTAL

3.1. Spray materials

Commercial agglomerated and sintered Cr_3C_2-37WC-18NiCoCrFe (WOKA 7502 and 7504: Oerlikon Metco AG, Wohlen, Switzerland) and Cr_3C_2-50NiCrMoNb powders (Amperit 595.059 and 595.074: H.C. Starck GmbH, Goslar, Germany) with Inconel 625-type metal matrix, and a plasma densified version of the common Cr_3C_2-25NiCr powder (WOKA 7302 and 7304: Oerlikon Metco AG, Wohlen, Switzerland) were

studied. Conventional agglomerated and sintered Cr_3C_2-25NiCr material (Amperit 588.059 and 584.072: H.C. Starck GmbH, Goslar, Germany) was also sprayed for comparison. Larger particle sizes (-38+10 or -45+15 µm) of the powders were used for HVOF spraying due to the higher process temperature compared to HVAF. Finer particle sizes (-30+5 or -30+10 µm) were used with HVAF spraying. The details of the powders are listed in **Table 1**.

Table 1 Details of the powders, processes used, sample coding and nominal particle size distribution

Sample code	Spray process	Manufacturing process	Powder composition [wt%]	Particle size [µm]	Powder manufacturer
CC1.1	HVOF	A&S	Cr_3C_2-25NiCr	-38+10	H.C. Starck
CC1.2	HVAF	A&S	Cr_3C_2-25NiCr	-30+10	H.C. Starck
CC2.1	HVOF	A&S, densified	Cr_3C_2-25NiCr	-45+15	Oerlikon Metco
CC2.2	HVAF	A&S, densified	Cr_3C_2-25NiCr	-30+10	Oerlikon Metco
CC625.1	HVOF	A&S	Cr_3C_2-50NiCrMoNb	-45+15	H.C. Starck
CC625.2	HVAF	A&S	Cr_3C_2-50NiCrMoNb	-30+5	H.C. Starck
CW1	HVOF	A&S	Cr_3C_2-37WC-18NiCoCrFe	-45+15	Oerlikon Metco
CW2	HVAF	A&S	Cr_3C_2-37WC-18NiCoCrFe	-30+10	Oerlikon Metco

A&S = Agglomerated and sintered

3.2. Coating manufacturing

Coatings were sprayed with commercial HVOF and HVAF guns, DJH2700 (Oerlikon Metco, Wohlen, Switzerland) and M3 (Uniquecoat Technologies LLC, Oilville, United States), respectively. The spray parameters are given in **Table 2**. It is worth noting that the HVAF system is pressure controlled and therefore the air and fuel parameters are given in pressure (bar). Coatings were sprayed on 5 mm-thick low carbon steel substrates (S235) measuring 200x50 mm, which were grit-blasted prior to spraying with mesh

36 alumina (Al_2O_3) grit. Target coating thickness was 300 µm. A long combustion chamber and a 4L2 nozzle were used for the HVAF spraying of the powders.

Table 2 Spray parameters used in HVAF and HVOF processes

Parameter	HVAF	HVOF
Oxygen	-	240 slpm
Air	7.4 bar	383 slpm
Fuel1 (propane)	7.0 bar	70 slpm
Fuel2 (propane)	7.3 bar	-
Spray distance	300 mm	230 mm
Surface speed	1.9 m/s	0.8 m/s
Pass spacing	4 mm	5.4 mm
Powder feedrate	130-200 g/min	60 g/min

3.3. Spray diagnostics

Average particle velocities and temperatures were measured with the Spraywatch 4s camera (Oseir Ltd, Tampere, Finland), positioned laterally and oriented perpendicularly to the spray stream. The distance of the camera from the spray stream was 75 mm, which resulted in a measurement volume of 34.4 x 26.3 x 5 mm. All measurements were carried out at the corresponding spray distance of the respective deposition process, i.e. 230 mm for HVOF and 300 mm for HVAF. Exposure times of 3 µs and 2 µs were used for the HVOF and HVAF spray processes, respectively. Shorter exposure time was used for HVAF spray process to avoid excessive particle overlapping due to the higher particle velocity, i.e. longer particle traces.

3.4. Characterization

All metallographic samples were prepared with the same sequential procedure of grinding with P220, P600 and P1200 SiC papers and polishing with 3, 1 and 0.25 µm diamond suspensions. Microstructures of the

coating cross sections were characterized with Scanning Electron Microscope (SEM: XL-30, Philips, Amsterdam, Netherlands) equipped with Energy Dispersive Spectrometer (EDS: EDAX Inc., Mahwah, United States). Ten SEM images of the coating and powder microstructure were used for image analysis to measure the volume percentages of pores, matrix, chromium carbides and optionally tungsten carbides. Segmentation and analysis of the SEM images was carried out with ImageJ. The EDS spectrum of each as-sprayed coating cross section was collected from an area of 190x140 µm. Detailed elemental line scans were performed on polished coating top surfaces with Field Emission Scanning Electron Microscope (FE-SEM: Zeiss Crossbeam 540, Carl Zeiss AG, Oberkochen, Germany) equipped with the EDS XMax^N 80 mm^2 silicon drift detector (SDD: Oxford Instruments, Oxfordshire, United Kingdom). Due to the small atomic number of carbon (Z=6) its determination with EDS is problematic and inaccurate. Therefore, the carbon and oxygen content of the feedstock powders and as-sprayed coatings were measured with LECO CS-230 carbon/sulphur analyser (LECO Corporation, St. Joseph, Michigan, USA). The EDS measurements of the as-sprayed coatings, including only metallic alloying elements, were corrected based on the carbon and oxygen content measured with the LECO CS-230. The combined weight percentage of carbon and oxygen was proportionally deducted from the weight percentage of each metallic element included in the EDS measurement to attain a normalised chemical composition for each coating.

Depth-sensing nanohardness measurements (NHT, Anton Paar TriTec, Peseux, Switzerland) were carried out according to the ISO14577 standard (Ref 28), by performing 200 indentations on each of the polished cross-sections with a Berkovich diamond indenter calibrated against a fused silica standard (Ref 29). Test conditions included a maximum load of 15 mN, a loading/unloading rate of 22 mN/min (corresponding to loading/unloading times of about 40 s), and a holding time of 15 s at maximum load. Indentation hardness values (H_{IT}) were obtained as the ratio of the applied load to the projected contact area, determined from the indenter contact depth using the calibrated indenter area function according to the Oliver-Pharr method (Ref 30). The Vickers hardness number, defined as the ratio of the applied load to the actual contact area,

was also computed through an approximate conversion of the projected to the actual contact area, in order to allow comparison of nanoindentation results with the Vickers hardness measurements described below. Specifically, hardness measurements with 300 gf (≈2.98 N) load and 10 s loading time were done on the coating cross sections with Vickers microhardness indenter MMT-X7 (Matsuzawa, Akita, Japan). Ten indentations were measured and an average hardness value was calculated for each coating. Fracture toughness of the coatings was determined by measuring seven Vickers indentations with Duramin-A300 (Struers ApS, Ballerup, Denmark) hardness indenter by using 5 kgf (≈49.03 N) load and 10 s loading time. Fracture toughness (K_{1C}) values were calculated by applying the Evans and Wilshaw's equation, **Equation 1** (Ref 31):

$$K_{1C} = 0.079\left(\frac{P}{a^{1.5}}\right)\log\left(4.5\frac{a}{c}\right) \quad (1)$$

where P is the load, a is the average half diagonal of the indentation and c is the average crack length.

X-ray diffraction (XRD) patterns of the spray powders and sprayed coatings were measured with Empyrean X-ray diffractometer (PANalytical, Almelo, Netherlands), using Cu-K_α radiation source with 40 mA current and 45 kV voltage.

4 RESULTS AND DISCUSSION

4.1. Spray diagnostics and carbon loss

The results of the spray diagnostic measurements are presented in **Table 3**. The measured particle temperatures for HVOF sprayed materials were 300-400 °C higher than with the HVAF spray process when measured at the corresponding spray distances (230 mm and 300 mm). The measured particle temperatures produced by the HVAF spray process are well below the melting point of pure Cr_3C_2 (1829 °C), although the latter phase might experience a limited degree of melting as it forms a deep eutectic at 1249 °C together

with Ni (Ref 32). The higher particle temperatures of 1750-1830 °C for HVOF, on the other hand, suggest that direct carbide melting can take place during spraying. The main reason for the higher particle temperature in the HVOF spray process is the higher combustion temperature. The particle velocities, on the other hand, are 200-300 m/s higher with the HVAF process compared to the HVOF process. Despite the higher particle velocity, the kinetic energies of the individual particles are higher for HVOF spraying due to the larger particle size, i.e. mass. The difference between the two deposition processes and the kinetic energy component of the sprayed material can be better described by dividing the particle's kinetic energy with its volume to get the kinetic energy density of the sprayed material. As a result, the measured increase in particle velocity for HVAF spray process produced 50 to 90 percent higher kinetic energy densities (J/m^3) of the sprayed material, **Equation 2**:

$$U = \frac{E_p}{V_p} = \frac{\frac{1}{2}\bar{m}_p\bar{v}_p^2}{V_p} = \frac{1}{2}\bar{\rho}_p\bar{v}_p^2 \quad (2)$$

where U is the energy density in (J/m^3), $E_p = \frac{1}{2}\bar{m}_p\bar{v}_p^2$ is the average kinetic energy of the particles, m_p is the average mass of the particles, $\bar{\rho}_p$ is their average density, v_p their average velocity, and V_p their average volume. Such increase surely plays an important role in producing denser coating structures combined with the fact that smaller particles, i.e. building blocks, are used to deliver the energy. This resulted in significantly improved performance in open circuit potential tests carried out in our previous study (Ref 27).

Table 3 Measured average particle temperatures and velocities, and measured carbon and oxygen content of the powders and as-sprayed coatings

Sample code	Process	T (stdev) [°C]	v (stdev) [m/s]	C_{powder} [wt%]	$C_{coating}$ [wt%]	C loss [%]	O_{powder} [wt%]	$O_{coating}$ [wt%]
CC1.1	HVOF	1850 (19.2)	704 (70.8)	11.7	8.5	27.4	0.27	1.40
CC1.2	HVAF	1470 (6.32)	944 (71.3)	11.8	8.9	24.6	0.05	0.66
CC2.1	HVOF	1750 (8.95)	668 (57.9)	10.6	9.9	6.6	0.21	0.49
CC2.2	HVAF	1440 (6.38)	927 (41)	11.0	9.8	10.9	0.05	0.43
CC625.1	HVOF	1770 (8.68)	767 (40.5)	7.3	6.6	9.6	0.05	0.89
CC625.2	HVAF	1460 (8.52)	949 (109)	7.6	6.4	15.8	0.05	0.89
CW1	HVOF	1830 (8.04)	666 (90.5)	9.1	8.5	6.6	0.06	0.47
CW2	HVAF	1410 (10.1)	905 (40.5)	9.2	8.1	12.0	0.11	0.63

(stdev = standard deviation)

The carbon content of the feedstock powders and the as-sprayed coatings was measured and the results are shown in **Table 3**. The highest amount of carbon was lost during the spraying of agglomerated and sintered Cr_3C_2-25NiCr powders (CC1.1 and CC1.2) by both HVOF and HVAF process, 27.4 and 24.6 %, respectively. The carbon loss with HVOF and HVAF processes was reduced down to 6.6 and 10.9 % (respectively) when the plasma densified powder was used. In most cases it appears that higher amount of carbon is lost during HVAF spraying even though the process temperature is lower. Reasons for this can be:

i) carbide rebounding, i.e. the rebounding of the rather large (≥ 2 μm) Cr_3C_2 grains from the deposited particles while they flatten, especially when carbides are poorly bonded to the surrounding matrix, according to the mechanism laid out in (Ref 33);

ii) selective deposition of particles with higher metallic matrix content, i.e. particles with high carbide content can easily bounce off the substrate due to insufficient ductility;

iii) increased carbon loss by in-flight oxidation as a result of longer dwell time and finer particle size, i.e. increased surface area. Indeed, the particle flight distance from the powder injector exit to the sprayed surface differs dramatically between the two processes. The particle flight distances with the hardware used in the current study were 310 and 715 mm for HVOF and HVAF spray processes, respectively.

However, high temperatures would also be needed, in addition to the finer particle size and longer dwell time in HVAF spraying, to melt the primary carbides within the sprayed particles to allow significant oxidation. Also, Li et al. (Ref 33) concluded that the carbon loss during HVOF spraying of Cr_3C_2-25NiCr via oxidation was very limited and the most significant carbon loss took place during particle impact and coating formation by carbide rebounding. This is indeed a more likely reason together with the selective particle deposition for the carbon loss during spraying with HVAF. This interpretation would also be consistent with the fact that the C loss is lower for the more ductile Cr_3C_2-50NiCrMoNb powder and for the plasma densified powder. In the former, the higher matrix content enhances the particles' ductility (avoiding selective deposition phenomena) and embeds more effectively the smaller carbide grains, preventing their rebounding. In the latter, the carbides are smaller and more intimately bound to the matrix (see the forthcoming Section 4.2.2).

4.2. Powder and coating microstructures

4.2.1. Cr_3C_2-25NiCr

The CC1.2 powder particles in **Fig. 1a** present the typical structure of agglomerated and sintered Cr_3C_2-25NiCr material with large Cr_3C_2 particles (1) embedded in the Ni20Cr metal matrix (2). The XRD pattern in **Fig. 1b** confirms the presence of the two-phase structure of orthorhombic Cr_3C_2 and cubic Ni-based metal matrix. The CC1.1 powder contained also Cr_7C_3 and the structure of the powder has been presented in a previous study (Ref 11).

The microstructures of the as-sprayed HVOF and HVAF CC1 coatings are presented in **Fig. 1c** and **Fig. 1d**, respectively. The HVOF sprayed coating in **Fig. 1c** contains string-like formations (pointed by arrows) in different grey levels as the result of dissolution and melting of the carbide particles during the high temperature processing. The different tones of grey arise from the Z-contrast of the BSE image, which shows the areas with higher molecular weight as brighter compared to the areas with increased carbon content. The average measured temperature of the HVOF sprayed particles in **Table 3** was 1850 °C while the HVAF sprayed particles only reached 1470 °C. As a result, the HVAF sprayed coating in **Fig. 1d** contains a large number of fine chromium carbide particles and shows almost no signs of carbide melting. Some brighter areas can be noticed in the microstructure (arrows in **Fig. 1d**), which represent areas with low carbon content, i.e. minimal carbide dissolution. The XRD pattern of the HVAF sprayed coating does not show any formation of secondary phases. However, due to the high number of diffraction peaks, and the peak broadening resulting from the high temperature process, it is difficult to distinguish all possible peaks accurately.

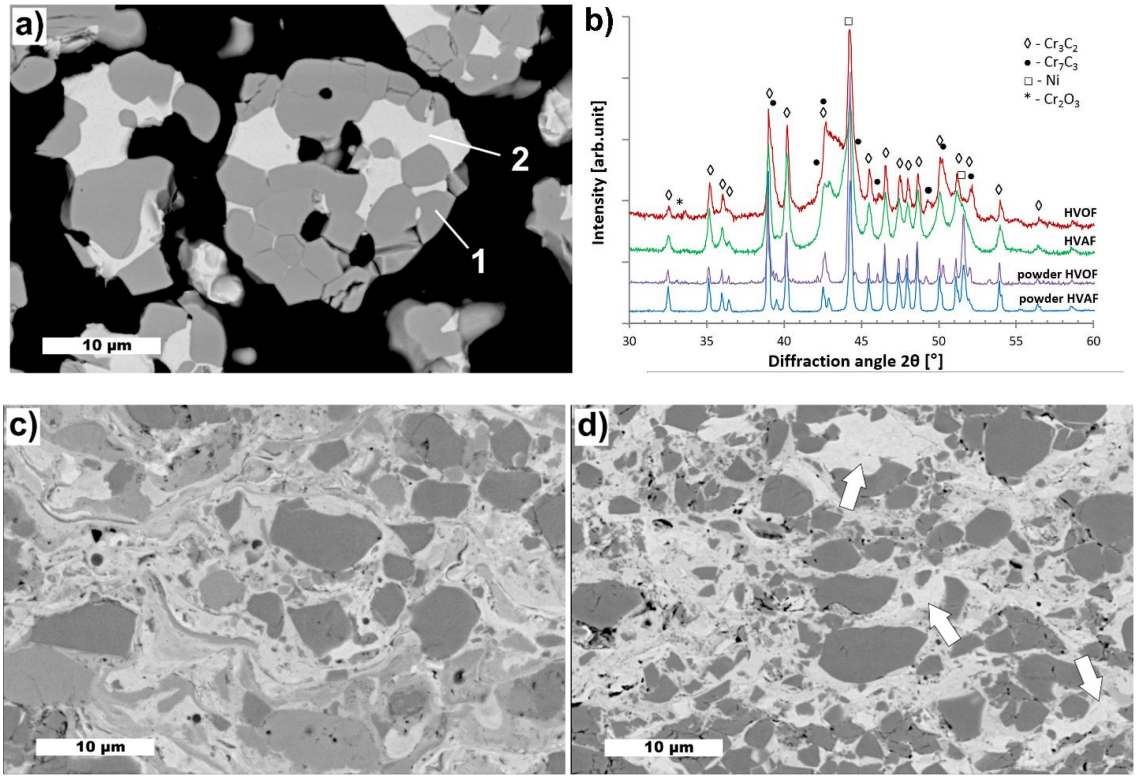

Fig. 1 a) The cross section BSE image of CC1.2 powder, b) the XRD patterns of the powders and as-sprayed coatings of CC1, c) the cross section BSE images of the HVOF sprayed CC1.1 coating and d) the HVAF sprayed CC1.2 coating

EDS line scan was carried out on the light grey and dark grey carbide particles observed in the HVOF sprayed CC1.2 coating structure in **Fig. 2a** to determine possible changes in composition. Based on the results in **Fig. 2b**, the light grey carbides consist of Cr, C and Ni, whereas the dark grey particles consist solely of Cr and C. Cr_7C_3 was detected in the XRD pattern and the light grey carbide structure is expected to be $(Cr,Ni)_7C_3$, which was recently reported also by Matthews (Ref 34). This is further supported by the fact that the solubility of Ni in Cr_3C_2 is minimal (Ref 32). Based on the EDS analysis, the Ni content of the light grey carbide was 7.6 wt% (assuming 30 at% C) and 0.9 wt% for the dark grey particle.

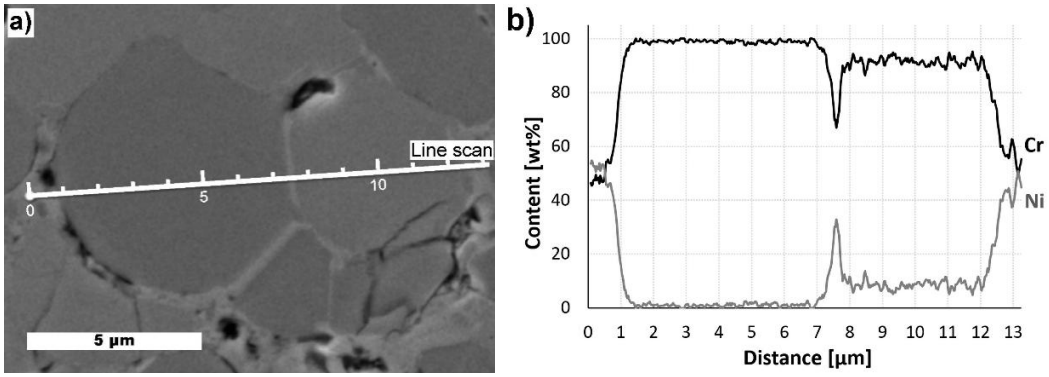

Fig. 2 a) Location of the EDS line scan over light grey and dark carbides (SE image) and b) resulting content of Cr and Ni

Based on the EDS area analysis presented in **Table 4**, the Ni content of both as-sprayed coatings was significantly higher compared to the nominal composition. It appears that the phenomenon is more pronounced in the case of the HVAF process with 6.6 wt% higher Ni content compared to HVOF. When compared to the nominal composition, where 20 wt% Ni content is expected, the measured 28.8 and 35.4 wt% Ni contents in HVOF and HVAF sprayed coatings would result in chromium carbide loss of 9.9 and 17.7 vol%, respectively. On the other hand, the measured carbon loss after spraying (**Table 4**) would nominally correspond to a chromium carbide loss of 22 vol% (3.2 wt% C) and 20 vol% (2.9 wt% C) for HVOF and HVAF sprayed coatings, respectively.

Table 4 Chemical composition of the HVOF sprayed CC1.1 and the HVAF sprayed CC1.2 coatings determined with EDS and image analysis results of the powders and coatings. Carbon content was measured with carbon analyser

	CHEMICAL COMPOSITION				IMAGE ANALYSIS			
	C	O	Cr	Ni	Porosity	Matrix	Cr_3C_2	Cr_3C_2
Sample	[wt%]				[vol% ± stdev]			size [µm]
CC1.1 coating	8.5	1.40	61.7	28.4	1.74 ±0.97	43.59 ±5.18	54.67 ±4.75	2.5
CC1.2 coating	8.9	0.66	55.3	35.2	1.46 ±0.47	43.47 ±3.31	55.07 ±3.19	2.1
CC1.1 powder	11.7	0.27	-	-	-	18.73 ±4.14	81.27 ±4.14	4.3
CC1.2 powder	11.8	0.05	-	-	-	16.81 ±2.28	83.19 ±2.28	5.0
Theoretical	10	-	70	20	-	20.8	79.2	-

Based on the image analysis, the actual loss of carbide grains was 24.5 and 24.1 vol% (**Table 4**) in HVOF and HVAF-sprayed coatings, respectively. The carbide loss estimates based on the Ni content (by EDS analysis) and on the C loss measurements are therefore closer to each other and to the actual value determined by image analysis in the case of the HVAF-sprayed coatings. In the HVOF-sprayed coatings, it seems that, in spite of the loss of carbides, much less C is lost from the coating.

This means that during the HVAF spraying process the carbides were mainly lost by complete removal, i.e. rebounding and selective particle deposition, thus favouring particles with high metal matrix content. Similar observations were done by Li et al. (Ref 33) in their study of carbide size effect on the carbide rebounding and carbon loss during HVOF spraying. They sprayed two types of Cr_3C_2-25NiCr powders with mean carbide sizes of 3.1 µm and 6.4 µm. The resulting coatings had reduced carbide sizes of 1.8 µm and 2.2 µm, and estimated Ni content of 31 and 39.4 wt%, respectively. The increased Ni content of 28.4 wt% in the current CC1.1 coating, sprayed with different HVOF equipment and powder, was not as high but showed a similar trend along with the reduced mean carbide size of 2.5 µm in the as-sprayed

coating compared to the 4.3 µm-size in the feedstock powder. The mean carbide size of the CC1.2 powder used for HVAF spraying was significantly larger, 5.0 µm, which resulted in carbide/particle diameter ratio of 0.29 calculated based on the mean carbide size and mean particle size of the powder. This is substantially higher than the value of 0.18 determined for the powder used by Li et al. (10-55 µm particle size and 6.4 µm mean carbide size). It becomes quite evident that if the HVAF sprayed particles are in partially melted state, i.e. with melted metal matrix, the carbide rebounding will be substantial due to the combination of coarse carbide size and thin splat thickness, which results in decreased carbide size and increased matrix content. However, if the particles are in solid state, i.e. softened just below the melting temperature, it can be expected that the carbide loss takes place through selective particle deposition rather than rebounding of individual carbides from the splat. The measured 1470 °C average particle temperature would in this case result in melted metal matrix and therefore carbide rebounding, which would be increased as the result of the higher particle velocity in **Table 3**. Additionally, it has to be kept in mind that the feedstock powder with fine particle size was used in HVAF spraying: the porous, agglomerated and sintered Cr_3C_2-25NiCr particles are light and fairly easily carried away by the high velocity gas stream.

In the case of HVOF spraying, the high particle temperature and resulting carbide dissolution and melting are more pronounced additional sources of carbide loss. When dissolution occurs, carbide grains are lost, but C remains in the coating as it is dissolved in the Ni-based matrix; hence, the assumption that carbide loss corresponds to direct carbon loss (which holds in the case of carbide rebounding and of selective deposition of matrix-rich powder particles) leads to a severe underestimation of the actual carbide loss.

Both coatings also contained fairly high amounts of porosity, which was often originating from cracked carbides and related pull-outs. Nevertheless, the HVAF sprayed CC1.2 coating contained lower amount of porosity compared to CC1.1.

4.2.2. Cr_3C_2-25NiCr (densified)

The plasma densification process used for CC2 powders rapidly heats and melts the agglomerated and sintered particles to create round, dense and well-flowing particles. SEM images formed by secondary electrons (SEs) of both CC2 feedstock powders are presented in **Fig. 3**. The morphology indicates that the CC2.1 powder in **Fig. 3a** contains more partially melted particles with typical agglomerated and sintered shape compared to the finer CC2.2 powder in **Fig. 3b**. This resulted also in higher mean carbide size of 3.6 µm for the CC2.1 powder compared to the CC2.2 powder with 2.2 µm size. The particle microstructure depends on the degree of melting during the densification process, which can produce partially or completely melted particles. The latter condition results in fine network-like structure of precipitating carbides with narrow areas of surrounding metal alloy binder (**Fig. 4a**, particle on the right**)**. Some of the original primary carbides also contained cracks similar to the previous agglomerated and sintered powders. Partially melted particles, on the other hand, still contain the original large primary carbides of the agglomerated and sintered powder with rounded edges and larger areas of metallic binder between the carbides (**Fig. 4a**, particle on the left**)**.

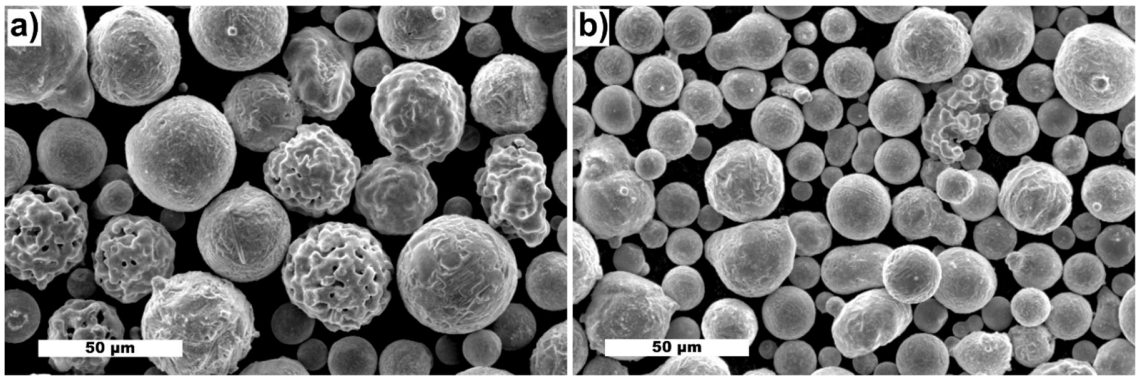

Fig. 3 SEM images (SE) of a) the CC2.1 and b) CC2.2 powders showing the larger amount of partially melted particles for the larger CC2.1 powder

As these unmelted particles, containing the original large primary carbides in the structure, were more numerous in the coarser CC2.1 powder, they also show up in the final sprayed coating. In such case, the metal matrix surrounding the large carbides can remain less affected by the carbide dissolution. This is seen as whiter areas (pointed by arrows) in the microstructure of the HVOF sprayed CC2.1 coating in **Fig. 4c**. Other areas of the coating are showing significant carbide dissolution creating carbon-saturated areas, which decreases locally the coating ductility and increases the risk of crack propagation initiated by an internal or external stress. By contrast, the majority of the particles from the finer size distribution (CC2.2) were completely melted by the plasma processing and formed fine carbide structures, which are retained in the HVAF-sprayed coating of CC2.2 in **Fig. 4d**.

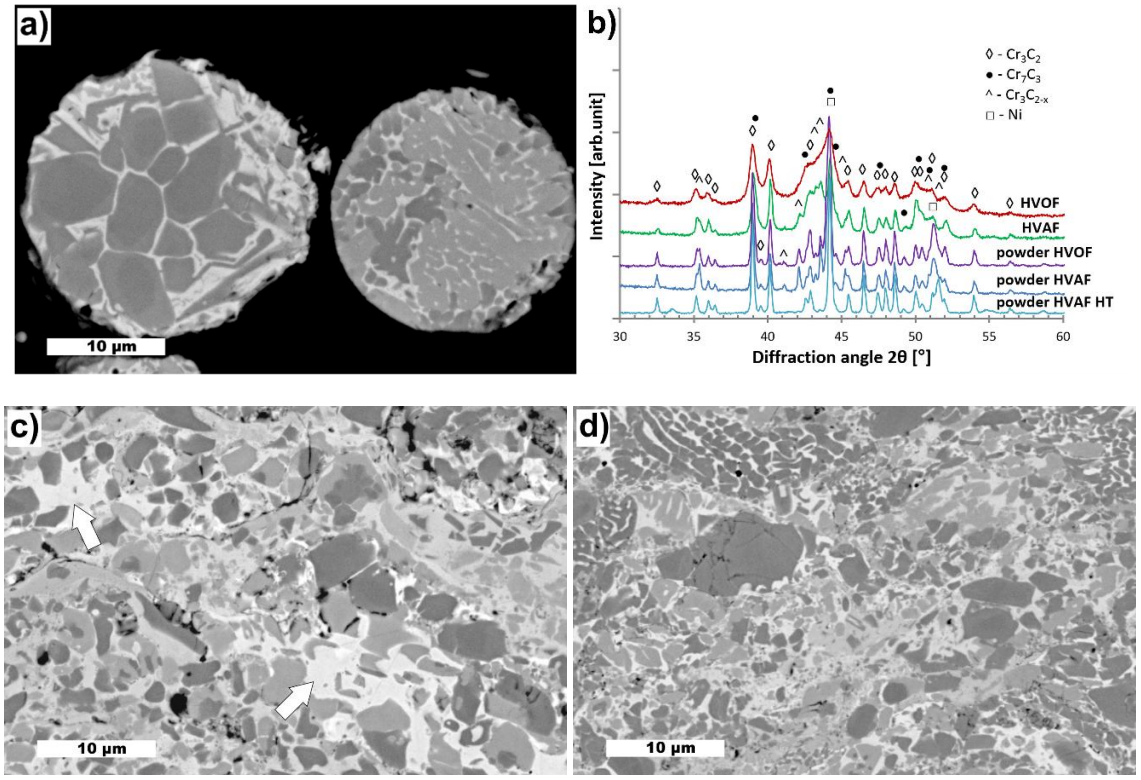

Fig. 4 a) The cross section BSE image of CC2.2 powder, b) the XRD patterns of the powders and as-sprayed coatings of CC2, c) the cross section BSE images of the HVOF sprayed CC2.1 coating and d) the HVAF sprayed CC2.2 coating

The XRD analysis of the plasma densified powder CC2 (in **Fig. 4b**) revealed the presence of Cr_7C_3 and metastable Cr_3C_{2-x}, where $0 \leq x \leq 0.5$. The formation of Cr_7C_3 takes place during the densification process, when the particles are melted and carbide dissolution, i.e. transfer of carbon from the Cr_3C_2 particles into the matrix, can take place (Ref 32,35). The formation of the metastable Cr_3C_{2-x} structure from amorphous Cr_3C_2 has been reported previously by Bouzy et al. (Ref 36), and it may be due to the conditions of the plasma densification process, involving rapid heating and cooling. The finer CC2.2 powder showed higher peak intensities for the Cr_3C_{2-x} phase compared to the CC2.1. This indicates higher content due to overall higher degree of melting during the densification process, also observed from the powder morphology in **Fig. 3**. Transformation of the metastable phase into stable chromium carbide form took place during a heat treatment of the CC2.2 powder at 700 °C for 14 hours (powder HVAF HT in **Fig. 4b**).

EDS line scan was done in order to differentiate between the two dominant greyscale contrast levels of the carbides present in **Fig. 5a**. The results in **Fig. 5b** confirm that the dark carbides consist of Cr and C, while the light grey carbide contains 11.6 wt% Ni replacing Cr, when C is excluded from the analysis. The structure of the light grey carbide is presumably M_7C_3 with a significant amount of Cr being substituted by Ni to form $(Cr,Ni)_7C_3$, similar to the CC1.1 coating. The metastable Cr_3C_{2-x} structure could not be identified reliably through the SEM images. It is quite clear that, due to the presence of various phases and several heat treatment cycles (sintering, plasma densification and spraying), there can be varying amounts of Ni present in the carbides.

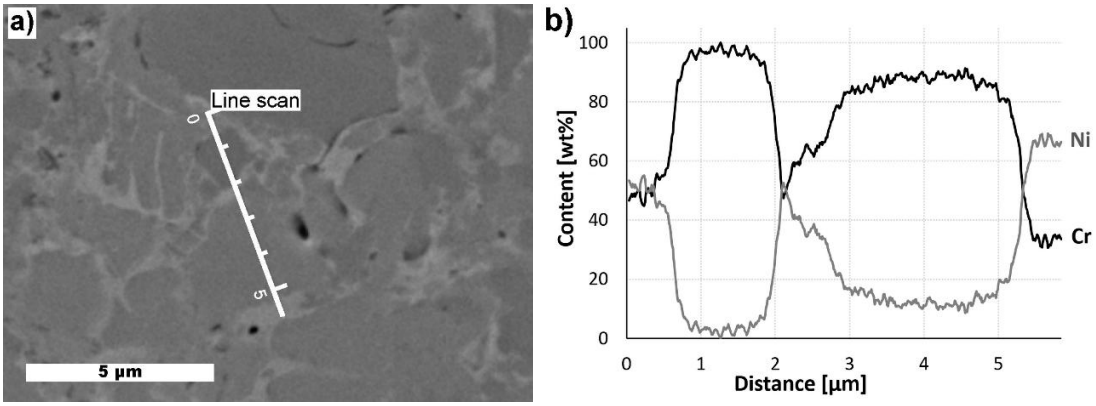

Fig. 5 a) Location of the EDS line scan over light grey and dark carbides (SE image) and b) resulting content of Cr and Ni

Measured carbon losses for HVOF and HVAF sprayed CC2 coatings were 0.7 and 1.2 wt% which corresponded to 4.7 and 8.1 vol% loss of Cr_3C_2, respectively. Based on the image analysis results in **Table 5**, the carbide loss in the as-sprayed coatings were 18.1 (HVOF) and 9.1 vol% (HVAF) compared to the nominal composition of 75Cr_3C_2-25(Ni20Cr). The difference between the image analysis results and the measured carbon loss indicates, once again, high carbide dissolution during HVOF spraying. On the other hand, carbide rebounding and/or selective particle deposition (which lead to direct carbon loss) are the dominant mechanisms in the HVAF sprayed coating, but they are not as extensive as with the CC1 coatings. The carbon loss and carbide loss in the HVAF sprayed CC2.2 coating are, indeed, both lower than in sample CC1.2, testifying to a lower occurrence of rebounding phenomena. This was further confirmed by the measured Ni contents of 23.8 wt% and 24.3 wt% for the HVOF and HVAF sprayed coatings, respectively. The measured mean carbide sizes of the CC2.1 and CC2.2 powders were 3.6 and 2.5 µm respectively, which is significantly smaller compared to the CC1.1 and CC1.2 powders. The round particle shape, more homogenous carbide distribution and finer carbide size were the main reasons for the reduced loss of carbides, complying with the findings of Li et al. in (Ref 33). Consequently, the finer carbide size seemed to have a substantial effect on the degree of carbide dissolution during the HVOF spraying.

Table 5 Chemical composition of the HVOF sprayed CC2.1 and the HVAF sprayed CC2.2 coatings determined with EDS and image analysis results of the powders and coatings. Carbon content was measured with carbon analyser

	CHEMICAL COMPOSITION				IMAGE ANALYSIS			
	C	O	Cr	Ni	Porosity	Matrix	Cr_3C_2	Cr_3C_2
Sample	[wt%]				[vol% ± stdev]			size [µm]
CC2.1 coating	9.9	0.49	66.0	23.6	2.18 ±0.41	36.74 ±4.69	61.08 ±4.82	2.2
CC2.2 coating	9.8	0.43	65.6	24.2	1.05 ±0.73	28.84 ±3.66	70.11 ±3.66	1.6
CC2.1 powder	10.6	0.21	-	-	-	20.57 ±4.38	79.43 ±4.38	3.6
CC2.2 powder	11.0	0.05	-	-	-	22.69 ±4.72	77.31 ±4.72	2.5
Theoretical	10.0	-	70.0	20.0	-	20.8	79.2	-

4.2.3. Cr_3C_2-50NiCrMoNb

The cross section of the CC625 powder appeared to contain a significant number of porous particles and some primary carbides with cracks, seen in **Fig. 6a**. The carbide particles exhibited different greyscale contrast levels in SEM images formed by backscattered electrons (BSEs). This difference originates again from the Z-contrast in the BSE images and light grey areas (1) in the chromium-based carbides are caused by increased atomic mass compared to the dark areas (2), either through the replacement of Cr with Ni/Mo, or through the formation of Cr_7C_3, i.e. decreased amount of carbon compared to Cr_3C_2. Indeed, significant presence of Cr_7C_3 was detected in the XRD patterns in **Fig. 6b**. A detail of the measured pattern of the CC625.2 powder (circle markers) with Lorentzian peak fit is presented in **Fig. 7**. The pattern shows the Cr_3C_2 (JCPDF 35-0804) peak of 100% relative intensity at 38.75° and the Cr_7C_3 (JCPDF 36-1482) peak of 33% relative intensity at 38.95°. The difference between the peak intensities confirms the significant presence of Cr_7C_3, which appears to be the major carbide phase in the powder. In addition, both peaks shifted to lower diffractions angles by approximately 0.19°, which could be caused by partial substitution

of Cr with other elements, e.g. Mo or Ni. The XRD patterns show also the presence of NbC, which can be seen in the particle cross section as small white precipitates (3) within the metallic matrix (**Fig. 6a**). The carbides could be pre-existing in the Ni-based raw material employed for the agglomeration and sintering process, as they may have been formed during the alloy solidification, when the remaining liquid becomes rich/saturated in Nb and C (Ref 37). Alternatively, they could have been developed during the sintering process in the presence of carbon. The XRD patterns of the as-sprayed coatings contain visible peaks of the Ni-based alloy matrix at 44.2° and 51.5° indicating areas that were not affected by the carbide dissolution. However, a broad band located approximately between 42° and 45° in the XRD patterns of both coatings suggests the presence of nanocrystalline or amorphous phase due to melt quenching and/or to severe plastic deformation in the solid state (the latter phenomenon being more likely during the HVAF process).

The microstructures of the as-sprayed HVOF and HVAF CC625 coatings are presented in **Fig. 6c** and **Fig. 6d**, respectively. The result of the lower particle temperature of the HVAF spray process (**Table 3**) can be observed as many of the fine carbides in the coating structure are still present. Namely, the HVAF sprayed coating CC625.2 in **Fig. 6d** shows significantly larger amount of fine primary carbide particles, having smaller sizes and sharper edges, indicating the lower particle temperature of the HVAF process and possible breaking during the impact. The HVOF sprayed coating, on the other hand, has experienced more pronounced carbide dissolution and melting of the carbide particles, whose edges are rounded and elongated (**Fig. 6c)**. Moreover, the BSE image of the CC625.1 coating structure shows metal matrix areas with different grey levels as a result of carbide dissolution (arrows in **Fig. 6c**), similar to CC1.1 coating. This feature can be seen, to a lower extent, in the CC625.2 coating as well. These structural observations indicate that melting of the metal matrix has also taken place during the HVAF spray process.

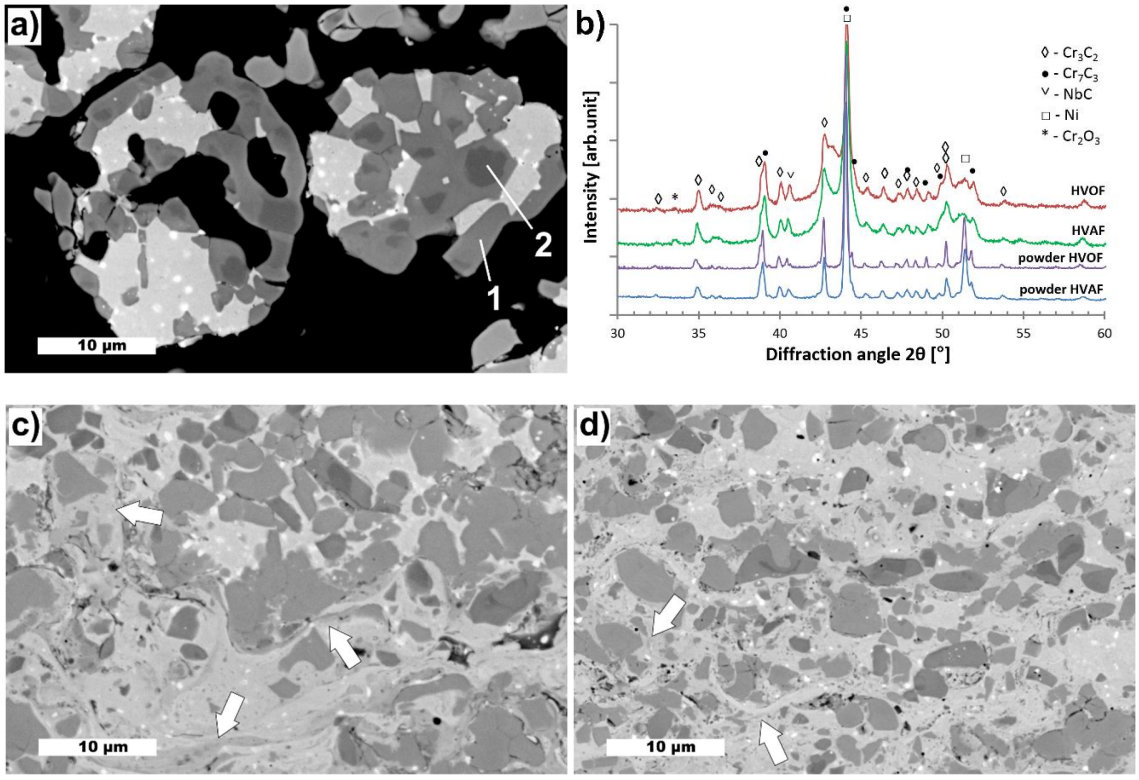

Fig. 6 a) The cross section BSE image of the CC625.2 powder, b) the XRD patterns of the powders and as-sprayed coatings of CC625, c) the cross section BSE images of the HVOF sprayed CC625.1 coating and d) the HVAF sprayed CC625.2 coating

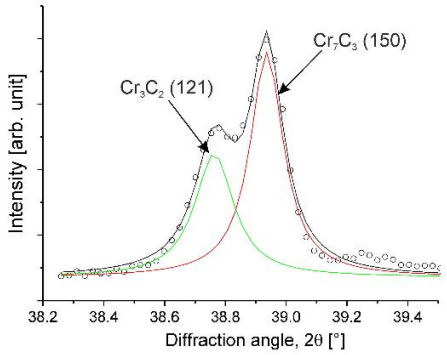

Fig. 7 A detailed section of the XRD pattern of CC625.2 powder showing the Cr_3C_2 (121) and Cr_7C_3 (150) peaks

According to the BSE images, both as-sprayed coatings contained identical dark and light grey carbide particles that were already observed in the feedstock powder (**Fig. 6a**). EDS line scan was performed on carbide particles with varying grey levels in **Fig. 8a** and the results in **Fig. 8b** show a variation in the amount of Ni between the two carbides. The light grey carbide contains a significant amount of Ni (11.0 wt%) while lower amount can be detected from the dark carbide (2.0 wt%), when carbon is excluded due to the above mentioned quantification inaccuracy. The high Ni content suggests that the light grey carbides indeed have M_7C_3 structure (Ref 34). This is supported by the high amount of light grey carbides present in the microstructure and high intensity of Cr_7C_3 peaks in the XRD patterns. The Mo content of the light and dark areas were 3.3 wt% and 5.6 wt%, respectively. Another line scan in **Fig. 8c** was performed on a carbide particle with light grey rim and dark center area. The results in **Fig. 8d** show that the Ni content of the whole carbide is low, approximately 1.6 wt% when C is excluded. Interestingly, the carbide rim seems to contain Mo, up to 10 wt%. The result indicates that some Cr in the carbide has been substituted by Mo, which is present in the metallic matrix. It has been reported that Mo has a solubility up to 5 and 15 at% in Cr_7C_3 and $Cr_{23}C_6$ at 1350 °C respectively, whereas no solubility in Cr_3C_2 was detected at this temperature (Ref 38). Therefore, it could be expected that the carbide rim structure is $(Cr,Mo)_7C_3$. On the other hand, the XRD patterns of the powders and coatings in **Fig. 6b** showed also shifting of the Cr_3C_2 XRD peaks to lower diffraction angles, which could be caused by an increase of the d-spacing of the carbide structure as a result of $(Cr,Mo)_3C_2$ phase formation at high temperature (Ref 39). Further transmission electron microscope studies are required to confirm the formed crystal structure.

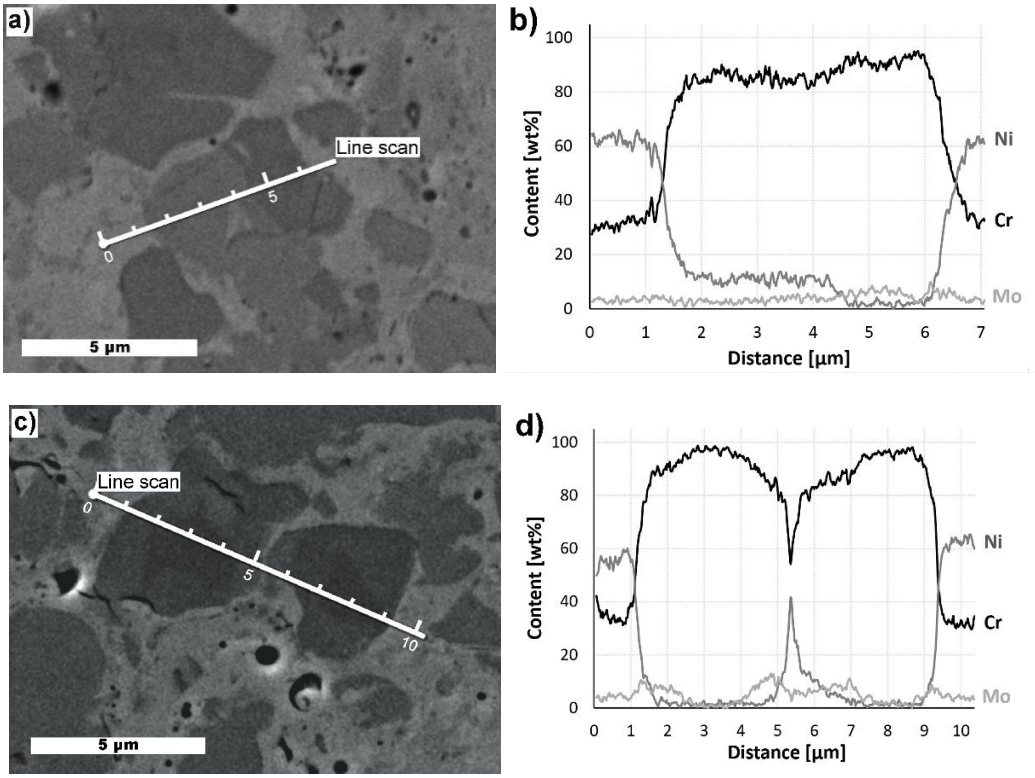

Fig. 8 Locations of the EDS line scans a) over light grey and dark carbides (SE image) and b) resulting content of Ni, Cr, and Mo, c) line scan over two carbides with dark centers (SE image) and d) resulting content of Ni, Cr, and Mo

Based on the image analysis results of the HVOF and HVAF sprayed CC625 coatings in **Table 6**, the lost carbide amounts compared to the nominal composition were 11.3 and 10.9 vol%, respectively. The measured carbon loss during spraying was 0.7 and 1.2 wt% for the same coatings, which corresponds to 5.2 and 9.1 vol% chromium carbides loss, assuming a pure Cr_3C_2 form for simplicity. Regardless of the approximation, the difference between the carbide loss from image analysis and the measured carbon loss is especially considerable for the HVOF coating, and, once again, it indicates that more pronounced carbide dissolution took place during the HVOF spraying, so that, in spite of the loss of carbide particles, some C was retained within the matrix. By contrast, carbide rebounding was again the dominant phenomenon in

HVAF spraying, where the carbide loss from image analysis and the measured carbon loss are closer to each other, consistent with the hypothesis put forward in Section 4.1. The unexpectedly high carbide content of the feedstock powder, based on image analysis, was originated by numerous particles that appeared to consist solely of carbides. Such particles would stay in the solid state during HVAF spraying and therefore would not adhere completely on the sprayed surface, but rather break up and form carbide fragments into the already formed metal matrix.

Table 6 Chemical composition of the HVOF sprayed CC625.1 and the HVAF sprayed CC625.2 coatings determined with EDS and image analysis results of the powders and coatings. Carbon content was measured with carbon analyser

	CHEMICAL COMPOSITION							**IMAGE ANALYSIS**			
	C	**O**	**Cr**	**Ni**	**Mo**	**Nb**	**Fe**	**Porosity**	**Matrix**	**Cr_3C_2**	**Cr_3C_2**
Sample	**[wt%]**							**[vol% ± stdev]**			**size [µm]**
CC625.1 coating	6.6	0.89	48.0	38.8	3.6	1.8	0.4	0.83 ±0.35	54.69 ±3.40	44.48 ±3.55	2.4
CC625.2 coating	6.4	0.89	47.6	37.5	4.7	2.4	0.5	0.52 ±0.29	54.60 ±3.90	44.88 ±3.93	2.1
CC625.1 powder	7.3	0.05	-	-	-	-	-	-	36.10 ±6.66	63.90 ±6.66	3.8
CC625.2 powder	7.6	0.05	-	-	-	-	-	-	35.38 ±5.42	64.62 ±5.42	2.1
Theoretical	-	-	-	-	-	-	-	-	44.2	55.8	-

4.2.4. Cr_3C_2-37WC-18NiCoCrFe

The CW powders (CW2 in **Fig. 9a**) contained similar differences in BSE image grey levels as the CC625 powder particles. Many chromium carbide particles consisted of a dark center area (1) with light grey rim (2), while others presented entirely the light grey color. In addition, the powder particles contained evenly distributed fine WC particles (3) within the alloy binder (4) and between the chromium carbide particles. The XRD analysis revealed strong peaks of WC and indicated the presence of both Cr_7C_3 and Cr_3C_2 (**Fig. 9b**). The peaks of Cr_3C_2 were slightly shifted, similar to the CC625 powders. The XRD analysis

did not reveal any compounds of $(Cr,W)_2C$ in the powders or coatings. This compound has been reported to exist in some WC-based agglomerated and sintered materials containing Cr_3C_2 (Ref 40).

The as-sprayed coatings contained the same phase structure as the powders. The peaks of the metallic matrix were significantly reduced compared to the feedstock powders. The microstructures of the HVOF sprayed CW1 and HVAF sprayed CW2 coatings are presented in **Fig. 9c** and **Fig. 9d**, respectively. The CW1 coating contains numerous large Cr_3C_2 particles while the HVAF sprayed CW2 coating seems to contain fewer and finer Cr_3C_2 particles. Moreover, the amount of metallic matrix seems to be higher for the HVAF sprayed coating.

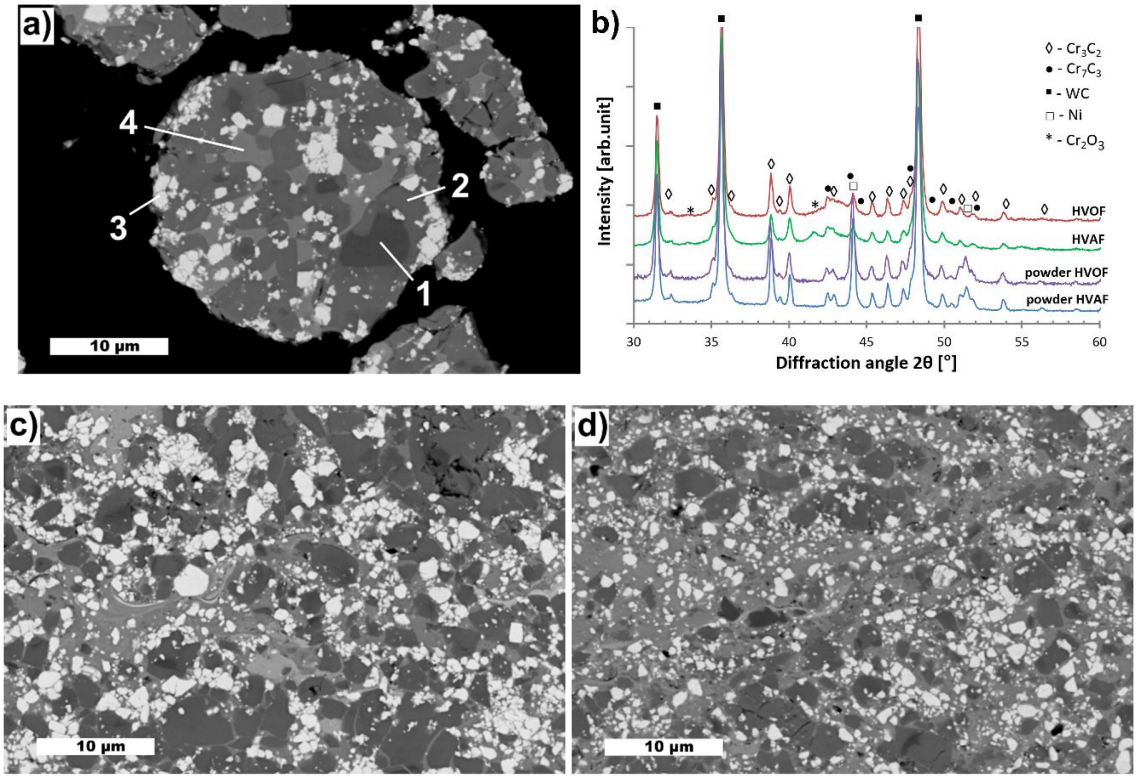

Fig. 9 a) The cross section BSE image of CW2 powder, b) the XRD patterns of the powders and as-sprayed coatings of CW1 and CW2, c) the cross section BSE images of the HVOF sprayed CW1 coating and d) the HVAF sprayed CW2 coating

EDS line scan was again carried out to analyse the compositional differences between the chromium carbides in **Fig. 10a**. The results in **Fig. 10b** reveal that the W content of the light grey area in the analysed carbide was 11.9 wt% (assuming 40 at% C), with a sharp drop when moving to the dark center area. The high intensity of the Cr_3C_2 phase compared to the Cr_7C_3 in the XRD pattern and the observed peak shift (-0.12°) support the replacement of Cr with W in the M_3C_2 structure, forming a $(Cr,W)_3C_2$ carbide structure (Ref 41,42). Indeed, the solubility of W has been reported to be up to 8.8 at% in Cr_3C_2 at 1350 °C (Ref 43). This time, the carbides did not contain any significant amount of Ni, different from all of the previous cases. This difference might be ascribed to the distinct chemical composition of the system, which could have favoured Cr substitution with W.

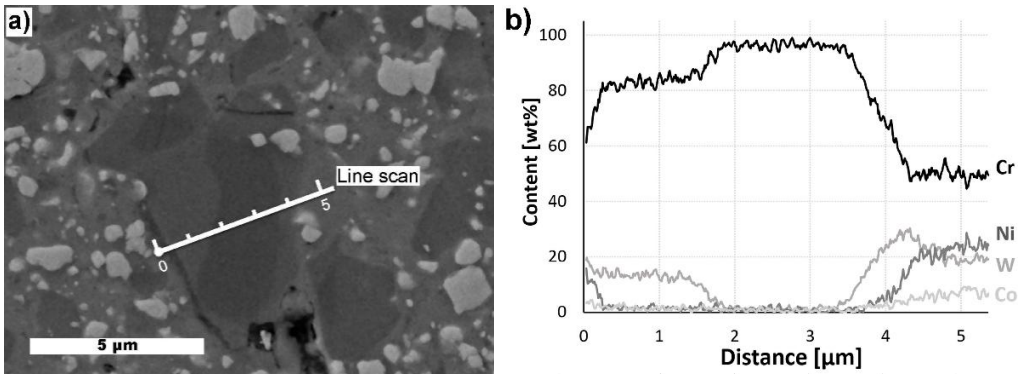

Fig. 10 a) Locations of EDS line scan over light grey and dark carbides (SE image) and b) resulting content of Cr, Ni, W and Co

Almost identical EDS area analyses were obtained from the HVOF and HVAF sprayed coatings (**Table 7**), which suggests that the deposition behaviour of both powders had been approximately the same for the two processes, i.e. no noticeable differences in the Ni or Co content. The Cr content in the CW1 coating was 2.2 wt% higher compared to the CW2 coating, whereas the W content was 2.5 wt% higher in the CW2 coating. This is further supported by the image analysis results that indicate significantly higher Cr_3C_2

content and lower WC content in the CW1 coating compared to CW2 coating. Also, the matrix content of the CW2 (47 vol%) coating is higher than CW1 (38 vol%), which differs significantly from the nominal content of approximately 18 vol%. The difference cannot be explained only by the carbon loss during spraying, although the latter was consistently higher for the HVAF sprayed CW2 coating (1.1 wt% or 9.9 vol% Cr_3C_2) compared to the HVOF sprayed CW1 coating (0.6 wt% or 5.4 vol% Cr_3C_2). Indeed, the feedstock powders already contained larger volume fraction of matrix compared to the nominal composition, which is transferred into the resulting coating microstructure. In addition, significantly higher standard deviation of matrix volume can be observed on the CW2 powder, which indicates the presence of particles with varying amounts of matrix. Deposition of particles with higher matrix content would be favoured especially in the HVAF spray process. Some error can be expected from the thresholding and calculation of several components from the coating structure. These results suggest, again, that Cr_3C_2 particles rebounded more extensively during HVAF spraying (it could be speculated, that Cr_3C_2-rich powder particles were not plastically deformable enough to be deposited by HVAF).

Table 7 Chemical composition of the HVOF sprayed CW1 and the HVAF sprayed CW2 coatings determined with EDS and image analysis results of the powders and coatings. Carbon content was measured with carbon analyser

Sample	CHEMICAL COMPOSITION							IMAGE ANALYSIS				
	C	O	Cr	Ni	W	Co	Fe	Porosity	Matrix	Cr_3C_2	WC	Cr_3C_2 / WC
	[wt%]							[vol% ± stdev]				size [µm]
CW1 coating	8.5	0.47	39.8	13.1	34.0	3.8	0.4	0.47 ±0.24	37.71 ±4.84	45.89 ±4.66	15.94 ±2.17	1.6 / 0.7
CW2 coating	8.1	0.63	37.5	13.4	36.4	3.7	0.2	0.62 ±0.19	46.63 ±3.37	32.44 ±3.08	20.34 ±1.42	1.5 / 0.7
CW1 powder	9.1	0.06	-	-	-	-	-	-	26.56 ±3.25	57.17 ±3.48	16.27 ±2.75	2.0 / 0.9
CW2 powder	9.2	0.11	-	-	-	-	-	-	27.10 ±7.57	54.99 ±6.86	17.91 ±2.81	1.7 / 0.9
Theoretical	-	-	-	-	-	-	-	-	18.4	60.4	21.1	-

4.3. Mechanical properties

The mechanical properties of the coatings were studied by Berkovich nanohardness testing with a load of 15 mN and by micro-hardness testing with loads of 0.3 and 5 kgf, using the Vickers indenter, as described in Section 3.4.

The HVOF sprayed CC2.1 and CW1 coatings showed the highest deviations in both nanohardness and 300 gf-microhardness results (**Table 8**). High deviation indicates that the coating microstructure is more heterogeneous than that of the other coatings, with high point-to-point variations that are likely due to the presence of more numerous weak areas. These can originate from overheated particles with dissolved carbides, as they were detected in the microstructure (e.g. in **Fig. 4c**).

This is further confirmed by the fact that these coatings exhibit a continuous and remarkably large decrease in hardness across the three testing loads: the hardness values of these samples drop by 200-300 Vickers units at every increase of the testing load, whilst the other coatings usually show drops of ≤100 HV. A decreasing trend is typical for heterogeneous thermally sprayed coatings and is due to the increase of the tested area, i.e. larger indentation mark and larger area under the indenter (Ref 44). At high loads, in fact, it is very likely that each of the large indentation marks encompasses one or more of the weak areas mentioned above, resulting in a decrease in the measured hardness. Few small cracks were in fact detected in the microstructure of the CC2.1 coating, resulting from the brittleness that probably followed from significant carbide dissolution and increase of carbon content of the matrix, as discussed in Section 4.2.2.

The latter phenomena are, in turn, witnessed by the remarkably high nanohardness of this sample. With a carbon loss (**Table 3**) being relatively low despite a measurable loss of carbides, the sprayed particles making up the CC2.1 coating exhibit significant hardening (and embrittlement) of the matrix by dissolved C, in accordance with the considerations in Section 4.2.2. On the other hand, the loss of carbide particles (comparatively lower than that of CC1.1 and CC1.2 samples) is not so extensive as to compromise the intra-lamellar properties. As a result, low-load nanoindentation, which primarily reflects intra-particle features (Ref 11,24), returns a particularly high value.

The similar behaviour of the CW1 coating could also reflect the formation of brittle structures inside the coating, as well as its lower matrix content and much higher content of large (therefore, brittle) Cr_3C_2 particles, in comparison to the CW2 sample (richer in metal matrix and in fine WC particles), in accordance with the discussion in Section 4.2.4. These features would result in high nanohardness, but low hardness at higher loads, due to extensive failure of the brittle structures under a high-load indentation. Brittle behaviour and/or weaker cohesion of the CC2.1 and CW1 coatings are further supported by the fracture toughness values determined from the cracking behaviour of 5 kgf Vickers indentations.

Consistent with the previous observations, it is noted that the HVOF coatings exhibit higher nanohardness than the corresponding HVAF ones (**Table 8**), since, in all cases, their metal matrix phase is hardened (and embrittled) by a greater amount of dissolved carbon, as inferred from the systematic difference between the limited C loss and the comparatively greater carbide loss (Section 4.2). On the other hand, all HVAF coatings except for CC1.2 show higher fracture toughness values compared to the corresponding HVOF coatings. The structural performance of HVAF coatings is a result of lower degree of carbide dissolution and high particle impact velocity, leading to tighter interparticle bonding. The latter is also testified by the particularly limited load-sensitivity of the hardness values of the HVAF coatings (**Table 8**), which, in accordance with previous considerations, implies strong cohesion, with fewer hardened, embrittled spots. Finally, both CC625 coatings showed remarkably good resistance to cracking, which can be attributed to high matrix content and, probably, to the lower carbide dissolution due to overall lower carbide content.

Table 8 Results of nanohardness measurement (indentation hardness H_{IT}, designated according to ISO 14577, and corresponding Vickers hardness $HV_{0.0015}$) and of microhardness measurement with 300 gf ($HV_{0.3}$) and 5 kgf (HV_5) force Vickers indentations, and calculated indentation fracture toughness (K_{IC}) of the coatings

Sample	Nanohardness [H_{IT} 0.015/40/15/40], GPa	Nanohardness [$HV_{0.0015}$]	Microhardness [$HV_{0.3}$]	Microhardness [HV_5]	K_{IC} [MPa/m$^{1/2}$]
CC1.1	10.86 (±0.77)	1006 (±71)	938 (±79)	839 (±8)	3.45 (±0.37)
CC1.2	10.08 (±0.90)	933 (±83)	920 (±51)	808 (±11)	3.21 (±0.45)
CC2.1	14.03 (±1.23)	1300 (±114)	947 (±144)	653 (±38)	2.59 (±0.37)
CC2.2	10.59 (±0.77)	981 (±71)	958 (±69)	905 (±19)	4.57 (±0.27)
CC625.1	10.71 (±0.86)	992 (±79)	806 (±117)	753 (±19)	4.93 (±0.35)
CC625.2	9.68 (±0.89)	897 (±82)	885 (±58)	792 (±16)	5.25 (±0.38)
CW1	12.62 (±1.18)	1169 (±110)	934 (±195)	764 (±30)	3.36 (±0.48)
CW2	11.26 (±1.10)	1043 (±102)	1104 (±118)	1000 (±26)	4.98 (±0.35)

5. CONCLUSIONS

Four chromium carbide (Cr_3C_2)-based powders were sprayed with both HVOF and HVAF processes: agglomerated and sintered Cr_3C_2-25NiCr (CC1), agglomerated, sintered and plasma-densified Cr_3C_2-25NiCr (CC2), agglomerated and sintered Cr_3C_2-50NiCrMoNb (CC625) and agglomerated and sintered Cr_3C_2-37WC-18NiCoCrFe (CW). Coarser particle size distributions were used for the higher-temperature HVOF process and finer particle size for the HVAF spray process. The structure, microstructure and chemical composition of powders and coatings were analysed and compared to the theoretical compositions of the feedstock materials. Also, comparisons between the HVOF and HVAF sprayed coatings were carried out by structural analysis and by characterising the mechanical properties of the as-sprayed coatings. The following conclusions were made:

- The CC625 powders contained significant amounts of Cr_7C_3 in addition to Cr_3C_2, while CC2 and CW powders contained traces of the Cr_7C_3 carbide.
- Higher particle velocities and lower temperatures were measured for the HVAF spray process. As a result, coatings with lower porosity were produced.
- The carbide content in the spray powders was confirmed to correspond to the theoretical volume fraction determined from the chemical composition, except for the CW powders, which were found to contain higher amount of matrix than was expected.
- Significant decrease of carbide content was observed after spraying in all cases. The highest carbide content was maintained in the CC2.2 coating deposited from plasma densified Cr_3C_2-25NiCr feedstock by HVAF spraying. A comparison between the carbide content of the coatings (determined by image analysis) and their total carbon content has led to the conclusion that carbide loss is caused both by dissolution during high temperature spray processes (particularly during HVOF spraying) and by selective rebounding of carbide particles or of carbide-rich powder particles (both in HVOF and in HVAF spraying). It is therefore believed that the deposition of powder particles with high metal matrix content is favoured, especially in the lower temperature HVAF process.
- The HVAF sprayed coatings generally showed higher fracture toughness but lower nanohardness when compared to HVOF sprayed coatings. Higher nanohardness of the HVOF coatings is ascribed to carbon dissolution in the metal matrix, which is on the other hand believed to be a primary source of brittle structures that impair toughness. This occurs particularly in the case of the HVOF-sprayed CC2.1 and CW1 coatings.
- Both coatings of CC625 showed high resistance to cracking attributed to the high matrix content and limited carbide dissolution due to overall lower amount of chromium carbides.

6. ACKNOWLEDGEMENTS

This research was carried out as part of the DIMECC's (Digital, Internet, Materials & Engineering Co-Creation) Hybrid Materials program. We gratefully acknowledge the financial support from Tekes (the Finnish Funding Agency for Innovation) and the participating companies. The authors would also like to thank Mr. Mikko Kylmälahti of Tampere University of Technology (TUT) for his help with the spray processing of the coatings, MSc. Leo Hyvärinen (TUT) for carrying out the XRD measurements, and Mr. Andrea Staiano (UniMORE) for assistance with the analysis of nanoindentation data.

7. REFERENCES

1. Š. Houdková, F. Zahálka, M. Kašparová, and L.M. Berger, Comparative Study of Thermally Sprayed Coatings under Different Types of Wear Conditions for Hard Chromium Replacement, *Tribol. Lett.*, 2011, **43**(2), p 139–154.
2. J.M. Guilemany, N. Espallargas, J. Fernández, P.H. Suegama, and A.V. Benedetti, High-Velocity Oxyfuel Cr_3C_2-NiCr Replacing Hard Chromium Coatings, *J. Therm. Spray Technol.*, 2005, **14**(3), p 335–341.
3. P. Vuoristo, K. Niemi, A. Mäkelä, and T. Mäntylä, Abrasion and Erosion Wear Resistance of Cr_3C_2-NiCr Coatings Prepared by Plasma, Detonation and High-Velocity Oxyfuel Spraying, *Thermal Spray Industrial Applications*, C.C. Berndt and S. Sampath, Ed., June 20-24, 1994 (Boston, MA), ASM International, 1994, p 121–126.
4. R.F. Voitovich and E.A. Pugach, High-Temperature Oxidation Characteristics of the Carbides of the Group VI Transition Metals, *Sov. Powder Metall. Met. Ceram.*, 1973, **12**(4), p 314–318.
5. D. Toma, W. Brandl, and G. Marginean, Wear and Corrosion Behaviour of Thermally Sprayed Cermet Coatings, *Surf. Coatings Technol.*, 2001, **138**, p 149–158.
6. L.M. Berger, M. Woydt, and S. Saaro, Comparison of Self-Mated Hardmetal Coatings under Dry Sliding Conditions up to 600 °C, *Wear*, 2009, **266**(3–4), p 406–416.

7. V. Matikainen, G. Bolelli, H. Koivuluoto, P. Sassatelli, L. Lusvarghi, and P. Vuoristo, High-Temperature Sliding Wear Behaviour of Thermally Sprayed Cr_3C_2 -Based Coatings, *The 17th Nordic Symposium on Tribology – NORDTRIB 2016*, 2016, p 10.

8. L.M. Berger, Application of Hardmetals as Thermal Spray Coatings, *Int. J. Refract. Met. Hard Mater.*, Elsevier Ltd, 2015, **49**(1), p 350–364.

9. T.S. Sidhu, R.D. Agrawal, and S. Prakash, Hot Corrosion of Some Superalloys and Role of High-Velocity Oxy-Fuel Spray Coatings - a Review, *Surf. Coatings Technol.*, 2005, **198**, p 441–446.

10. A. Wank, B. Wielage, H. Pokhmurska, E. Friesen, and G. Reisel, Comparison of Hardmetal and Hard Chromium Coatings under Different Tribological Conditions, *Surf. Coatings Technol.*, 2006, **201**(5), p 1975–1980.

11. G. Bolelli, L.-M. Berger, T. Börner, H. Koivuluoto, V. Matikainen, L. Lusvarghi, C. Lyphout, N. Markocsan, P. Nylén, P. Sassatelli, R. Trache, and P. Vuoristo, Sliding and Abrasive Wear Behaviour of HVOF- and HVAF-Sprayed Cr_3C_2–NiCr Hardmetal Coatings, *Wear*, 2016, **358**–**359**, p 32–50.

12. S. Zimmermann, B. Gries, and B. Brüning, New Cermet Powders for HVOF Spraying with Improved Corrosion and Oxidation Resistance for Offshore, Mining and Power Generation Applications, *Therm. Spray Bull.*, 2011, **2**, p 94–100.

13. I. Hulka, V. a. A. Şerban, I. Secoşan, P. Vuoristo, and K. Niemi, Wear Properties of CrC–37WC–18M Coatings Deposited by HVOF and HVAF Spraying Processes, *Surf. Coatings Technol.*, 2012, **210**, p 15–20.

14. S. Zimmermann and H. Kreye, Chromium Carbide Coatings Produced with Various HVOF Spray Systems, *Thermal Spray: Practical Solutions for Engineering Problems*, C.C. Berndt, Ed., Oct 7-11, 1996 (Cincinnati, OH), ASM International, 1996, p 147.

15. R. Schwetzke and H. Kreye, Microstructure and Properties of Tungsten Carbide Coatings Sprayed with Various High-Velocity Oxygen Fuel Spray Systems, *J. Therm. Spray Technol.*, 1999, **8**(3), p 433–439.

16. B.R. Marple and R.S. Lima, Process Temperature/Velocity-Hardness-Wear Relationships for High-Velocity Oxyfuel Sprayed Nanostructured and Conventional Cermet Coatings, *J. Therm. Spray Technol.*, 2005, **14**(1), p 67–76.

17. J. Kawakita, H. Katanoda, M. Watanabe, K. Yokoyama, and S. Kuroda, Warm Spraying: An Improved Spray Process to Deposit Novel Coatings, *Surf. Coatings Technol.*, 2008, **202**(18), p 4369–4373.

18. S. Kuroda, M. Watanabe, K. Kim, and H. Katanoda, Current Status and Future Prospects of Warm Spray Technology, *J. Therm. Spray Technol.*, 2011, **20**(4), p 653–676.

19. B. Wielage, A. Wank, H. Pokhmurska, T. Grund, C. Rupprecht, G. Reisel, and E. Friesen, Development and Trends in HVOF Spraying Technology, *Surf. Coatings Technol.*, 2006, **201**(5), p 2032–2037.

20. V. Matikainen, K. Khanlari, A. Milanti, H. Koivuluoto, and P. Vuoristo, Spray Parameter Effect on HVAF Sprayed (Fe,Cr)C-30FeNiCrSi Hardmetal Coatings, *Thermal Spray: Fostering a Sustainable World for a better life!*, 2016, p 184–189.

21. A. Verstak and V. Baranovski, Activated Combustion HVAF Coatings for Protection against Wear and High Temperature Corrosion, *Thermal Spray 2003: Advancing the Science and Applying the Technology*, B.R. Marple and C. Moreau, Ed., May 5-8, 2003 (Orlando, FL), ASM International, 2003, p 535–541.

22. A. Verstak and V. Baranovski, AC-HVAF Sprayed Tungsten Carbide : Properties and Applications, *Thermal Spray 2006: Building on 100 Years of Success*, B.R. Marple, M.M. Hyland, Y.-C. Lau, R.S. Lima, and J. Voyer, Ed., May 15-18, 2006 (Seattle, WA), ASM International, 2006, p 643–648.

23. Q. Wang, S. Zhang, Y. Cheng, J. Xiang, X. Zhao, and G. Yang, Wear and Corrosion Performance of WC-10Co4Cr Coatings Deposited by Different HVOF and HVAF Spraying Processes, *Surf. Coatings Technol.*, Elsevier B.V., 2013, **218**(1), p 127–136.

24. G. Bolelli, L.M. Berger, T. Börner, H. Koivuluoto, L. Lusvarghi, C. Lyphout, N. Markocsan, V.

Matikainen, P. Nylen, P. Sassatelli, R. Trache, and P. Vuoristo, Tribology of HVOF- and HVAF-Sprayed WC-10Co4Cr Hardmetal Coatings: A Comparative Assessment, *Surf. Coatings Technol.*, Elsevier B.V., 2015, **265**, p 125–144.

25. A. Verstak, V. Baranovski, and U.S.A. Virginia, Deposition of Carbides by Activated Combustion HVAF Spraying, *Thermal Spray 2004: Advances in Technology and Application*, ASM International, May 10-12, 2004 (Osaka, Japan), ASM International, 2004, p 551-555.
26. L.-M. Berger, R. Trache, F.-L. Toma, S. Thiele, J. Norpoth, and L. Janka, Development of Cost-Effective Hardmetal Coating Solutions for High-Temperature Applications Part One - Feedstock Powders, Cost-Effectiveness and Coating Properties, *Therm. Spray Bull.*, 2015, **8**(2), p 126–135.
27. V. Matikainen, H. Koivuluoto, and P. Vuoristo, Microstructural Characteristics of Different Cr_3C_2 Coating Compositions Sprayed with HVOF and HVAF Processes, *28th International Conference on Surface Modification Technologies*, T.S. Sudarshan, P. Vuoristo and H. Koivuluoto, Ed., June 16-18, 2014 (Tampere, Finland), Valardocs, 2015, p 77–87.
28. "ISO 14577-1:2002 - Metallic Materials — Instrumented Indentation Test for Hardness and Materials Parameters — Part 1: Test Method," (Geneva, Switzerland), International Organization for Standardization (ISO), 2002.
29. "ISO 14577-2:2002 - Metallic Materials — Instrumented Indentation Test for Hardness and Materials Parameters — Part 2: Verification and Calibration of Testing Machines," (Geneva, Switzerland), International Organization for Standardization (ISO), 2002.
30. W. Oliver and G. Pharr, An Improved Technique for Determining Hardness and Elastic Modulus Using Load and Displacement-Sensing Indentation Systems, *J. Mater. Res.*, 1992, **7**(6), p 1564–1583.
31. A.G. Evans and T.R. Wilshaw, Quasi-Static Solid Particle Damage in Brittle solids - I. Observations Analysis and Implications, *Acta Metall.*, Pergamon, 1976, **24**(10), p 939–956.
32. T.Y. Velikanova, A.A. Bondar, and A. V Grytsiv, The Chromium-Nickel-Carbon (Cr-Ni-C) Phase Diagram, *J. Phase Equilibria*, 1999, **20**(2), p 125–147.

33. C.J. Li, G.C. Ji, Y.Y. Wang, and K. Sonoya, Dominant Effect of Carbide Rebounding on the Carbon Loss during High Velocity Oxy-Fuel Spraying of Cr_3C_2-NiCr, *Thin Solid Films*, 2002, **419**(1–2), p 137–143.

34. S. Matthews and L.-M. Berger, Long-Term Compositional/microstructural Development of Cr_3C_2-NiCr Coatings at 500°C, 700°C and 900°C, *Int. J. Refract. Met. Hard Mater.*, 2016, **59**, p 1–18.

35. M. Venkatraman and J.. Neumann, The C-Cr (Carbon-Chromium) System, *Bull. Alloy Phase Diagrams*, 1990, **11**(2), p 152–159.

36. E. Bouzy, E. Bauer-Grosse, and G. Le Caer, NaCl and Filled Re3B-Type Structures for Two Metastable Chromium Carbides, *Philos. Mag. B*, 1993, **68**(5), p 619–638.

37. J.N. Dupont, C. V. Robino, and A.R. Marder, Solidification and Weldability of Nb-Bearing Superalloys, *Weld. J.*, 1998, **77**(10), p 417s–431s.

38. A. Bondar, O. Dovbenko, V. Ivanchenko, and A. Kozlov, Carbon – Chromium – Molybdenum, *Refractory metal systems*, 2010, p 290–307.

39. V.N. Eremenko, T.Y. Velikanova, and A.A. Bondar, The Phase Diagram of the Cr-Mo-C System. II. Phase Equilibria in the Partial System Mo2C-Cr7C3-C, *Sov. Powder Metall. Met. Ceram.*, 1987, **26**(6), p 506–511.

40. L.-M. Berger, S. Saaro, T. Naumann, M. Kašparova, and F. Zahálka, Microstructure and Properties of HVOF-Sprayed WC-$(W,Cr)_2C$-Ni Coatings, *J. Therm. Spray Technol.*, 2008, **17**(3), p 395–403.

41. Y.Z. Jin, F.M. Ye, X.G. Zeng, and R.S. Yang, Carbothermal Synthesis of Cr_3C_2-WC-Ni Nanocomposite Powders, *Adv. Mater. Res.*, 2013, **661**, p 3–6.

42. Z. Tükör, W.D. Schubert, A. Bicherl, A. Bock, and B. Zeiler, Formation of W-Cr- Phases During the Production of Cr-Doped WC Powders, *17th Plansee Seminar*, (Reutte, Austria), 2009, p HM44/1-HM44/10.

43. A. Watson and A. Kroupa, Carbon – Chromium – Tungsten, *Refractory metal systems*, 2010, p 379–396.

44. J. Nohava, B. Bonferroni, G. Bolelli, and L. Lusvarghi, Interesting Aspects of Indentation and Scratch Methods for Characterization of Thermally-Sprayed Coatings, *Surf. Coatings Technol.*, 2010, **205**(4), p 1127–1131.